



Comprehensive defect suppression in perovskite nanocrystals for high-efficiency light-emitting diodes

Young-Hoon Kim^{1,2,10}, Sungjin Kim^{1,2,10}, Arvin Kakekhani^{3,10}, Jinwoo Park^{1,2}, Jaehyeok Park⁴, Yong-Hee Lee¹, Hengxing Xu⁵, Satyawan Nagane⁶, Robert B. Wexler³, Dong-Hyeok Kim^{1,2}, Seung Hyeon Jo^{1,2}, Laura Martínez-Sarti⁷, Peng Tan^{3,8}, Aditya Sadhanala^{6,9}, Gyeong-Su Park¹, Young-Woon Kim¹, Bin Hu⁵, Henk J. Bolink⁷, Seunghyup Yoo⁴, Richard H. Friend⁶, Andrew M. Rappe³✉ and Tae-Woo Lee^{1,2}✉

Electroluminescence efficiencies of metal halide perovskite nanocrystals (PNCs) are limited by a lack of material strategies that can both suppress the formation of defects and enhance the charge carrier confinement. Here we report a one-dopant alloying strategy that generates smaller, monodisperse colloidal particles (confining electrons and holes, and boosting radiative recombination) with fewer surface defects (reducing non-radiative recombination). Doping of guanidinium into formamidinium lead bromide PNCs yields limited bulk solubility while creating an entropy-stabilized phase in the PNCs and leading to smaller PNCs with more carrier confinement. The extra guanidinium segregates to the surface and stabilizes the undercoordinated sites. Furthermore, a surface-stabilizing 1,3,5-tris(bromomethyl)-2,4,6-triethylbenzene was applied as a bromide vacancy healing agent. The result is highly efficient PNC-based light-emitting diodes that have current efficiency of 108 cd A⁻¹ (external quantum efficiency of 23.4%), which rises to 205 cd A⁻¹ (external quantum efficiency of 45.5%) with a hemispherical lens.

Metal halide perovskites (MHPs) with the general ABX₃ formula (where A is an organic or inorganic cation, B is a metal cation and X is a halide anion) have narrow emission spectra (full-width at half-maximum ≈ 20 nm), allowing them to achieve high colour purity, a tunable emission wavelength range ($400 \text{ nm} \leq \lambda \leq 780 \text{ nm}$) and low-cost solution processability^{1–6}. As a result, MHPs have been regarded as promising light emitters^{5–12}. Such properties have also led to perovskite light-emitting diodes (PeLEDs), which have exhibited a tremendous increase in electroluminescence efficiency^{13–15}. These improvements have been obtained by (1) increasing the radiative recombination rate¹⁶ and (2) lowering the non-radiative recombination rate¹⁷. The radiative recombination rate of the charge carriers has been increased by spatially confining the electrons and holes in small perovskite polycrystalline nanograins³, low-dimensional crystals^{18–20} or colloidal perovskite nanocrystals (PNCs)^{4,5}. More effective strategies for suppression of defects and associated non-radiative recombination are required to surpass the state of the art and further increase the electroluminescence efficiency.

In perovskite polycrystalline bulk films, stoichiometric control of precursors³, use of passivation agents^{18–21} and post-treatments^{14,22,23} were shown to lead to a maximum current efficiency of 78 cd A⁻¹ (with an external quantum efficiency (EQE) of 20.3% ph/el based on Lambertian assumption)¹⁸. In colloidal PNCs, non-radiative

recombination and defects are reduced by surface-binding ligands; however, this strategy has limitations: (1) the dynamic nature of ligand–surface bonds and (2) steric hindrance effects that can leave undercoordinated sites unpassivated and prone to defect formation^{8,9}. B-site cation engineering¹⁰, X-site anion exchange¹¹ and surface-binding ligand engineering¹² have also been used, leading to a maximum current efficiency of 76.8 cd A⁻¹ (with an EQE of 17.1% ph/el) in green emission²⁴ and current efficiency of 10.6 cd A⁻¹ (EQE of 21.3% ph/el considering angular electroluminescence distribution) in red emission¹¹ in PeLEDs based on CsPbX₃.

The majority of research into PeLEDs is based on all-inorganic PNCs. It has been shown that the orientational freedom of the liquid-like dipoles associated with the organic cations can reduce the charge recombination rates^{25–28}. Although beneficial for photovoltaic applications, this is undesirable for LEDs²⁹. The all-inorganic MHPs contain spherical atomic A-site cations with zero dipole moment, leading to enhancement of charge recombination. Nevertheless, there are shortcomings associated with the atomic A-site cations: a small phase space for tunability and a lack of lattice-stabilizing directional hydrogen bonds. At the same time, there has been a lack of comprehensive material design strategies to passivate the surface defects and confine charge carriers inside of the nanocrystals.

Here we propose a simple and rational PNC design to simultaneously stabilize the undercoordinated sites at the surface while

¹Department of Materials Science and Engineering, Seoul National University, Seoul, Republic of Korea. ²School of Chemical and Biological Engineering, Institute of Engineering Research, Research Institute of Advanced Materials, Nano Systems Institute, Seoul National University, Seoul, Republic of Korea. ³Department of Chemistry, University of Pennsylvania, Philadelphia, PA, USA. ⁴School of Electrical Engineering, Korea Advanced Institute of Science and Technology, Daejeon, Republic of Korea. ⁵Department of Materials Science and Engineering, University of Tennessee, Knoxville, TN, USA. ⁶Cavendish Laboratory, University of Cambridge, Cambridge, UK. ⁷Instituto de Ciencia Molecular, Universidad de Valencia, Paterna, Spain. ⁸Department of Physics, Harbin Institute of Technology, Harbin, China. ⁹Clarendon Laboratory, Department of Physics, University of Oxford, Oxford, UK. ¹⁰These authors contributed equally: Young-Hoon Kim, Sungjin Kim, Arvin Kakekhani. ✉e-mail: rappe@sas.upenn.edu; twlees@snu.ac.kr

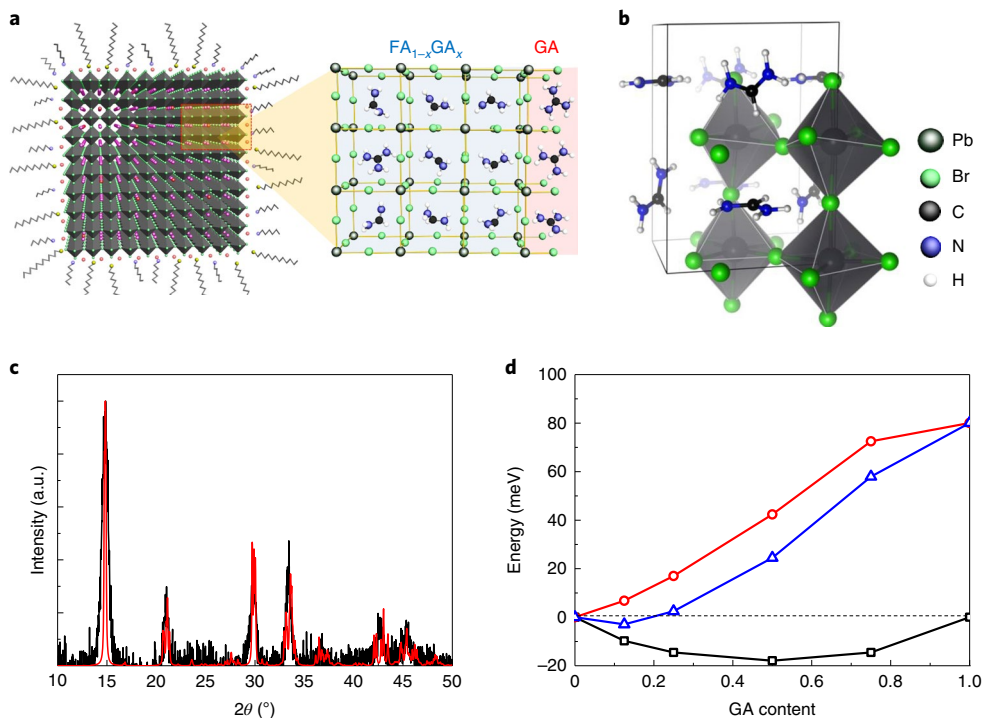


Fig. 1 | Structure of $\text{FA}_{1-x}\text{GA}_x\text{PbBr}_3$ PNCs. **a**, A schematic illustration of the ligand-stabilized $\text{FA}_{1-x}\text{GA}_x\text{PbBr}_3$ PNC structure. **b**, The modelled bulk crystal structure of FAPbBr_3 . **c**, Measured (black) and DFT-simulated (red) XRD patterns of FAPbBr_3 . **d**, Density functional theory formation energy (blue, relative to the precursors), internal (enthalpic) energy (red) and configurational entropic stabilization energy (black) of $\text{FA}_{1-x}\text{GA}_x\text{PbBr}_3$ crystals ($0 \leq x \leq 1$).

improving the confinement of charge carriers inside the nanocrystals by employing a zero-dipole guanidinium cation (CH_5N_3^+ ; GA^+)^{30,31}, which provides lattice-stabilizing effect via its hydrogen bonds. We exploit fine substitutional doping of formamidinium (CH_3N_2^+ ; FA^+) lead bromide (FAPbBr_3) by single GA^+ cations in colloidal PNCs instead of cation alloying approaches in perovskite polycrystalline bulk films that have been used in solar cells^{32,33}. The increased surface stability is driven by the extra amino group in the GA^+ due to its extra hydrogen bonds³⁴ and more uniformly distributed positive charges³⁵. Decylamine and oleic acid are also used as surface-binding ligands (Fig. 1a), providing an additional level of surface stabilization. We show that although adding guanidinium (GA) to the particle is penalized from an internal energy point of view due to its larger size, the gain in configurational entropy³⁶ stabilizes low concentrations of GA. We further reduce non-radiative recombination by applying 1,3,5-tris(bromomethyl)-2,4,6-triethylbenzene (TBTB) overcoat, which can heal the leftover halide vacancies. We ultimately achieved a current efficiency of 108 cd A^{-1} , further increased to 205 cd A^{-1} by employing a hemispherical lens.

Results

Structural properties. We begin by studying how GA doping influences the structure of FAPbBr_3 . We construct a computational model of FAPbBr_3 PNCs (see Supplementary Fig. 1 and the Methods for details). The fully ab initio-extended bulk model (Fig. 1b) can represent the FAPbBr_3 PNCs and reproduce their experimental X-ray diffraction (XRD) patterns (Fig. 1c). We calculate the formation free energy (from precursors) of $\text{FA}_{1-x}\text{GA}_x\text{PbBr}_3$ as x increases from 0 to 1, taking into account both enthalpic and configurational entropic contributions (Fig. 1d). Guanidinium is larger than FA and beyond the tolerance of the (lead-bromide-based) perovskite structure^{37–39}, therefore enthalpy does not preferentially drive GA to the inside of the perovskite. Nonetheless, small concentrations ($\sim 12.5\%$) of GA can still be dissolved in the structure due to entropy stabilization³⁶.

Beyond concentrations of $\sim 12.5\%$, enthalpy wins over entropy and drives the surplus GA to the surface of the PNCs.

As x is increased from 0 to 1, the size of $\text{FA}_{1-x}\text{GA}_x\text{PbBr}_3$ PNCs decreases from $\sim 10 \text{ nm}$ to $\sim 5.1 \text{ nm}$ (Fig. 2a and Supplementary Fig. 2). The decrease in size is also confirmed by observing a general trend for the relative increase of the peak intensity ratio (of the organic ligands to inorganic perovskite components) in the X-ray photoelectron spectroscopy measurements (see Supplementary Fig. 3 and the associated discussion for more details). Increasing the GA concentration increases the enthalpy of the bulk of the PNCs, thereby destabilizing them. To compensate for this energy penalty, the PNCs increase their surface-to-bulk ratio by decreasing their size. The PNCs are stabilized by the surrounding acid/amine ligands. In samples that lack GA, the optimal surface-to-bulk ratio is determined by the balance between surface formation energy cost and the stabilization imparted by surface-binding ligands. As can be seen in Fig. 2b,c, the latter is a result of both chemical point interactions and dispersion interactions (involving alkyl and alkenyl groups). The point interactions involve the acid ($-\text{COOH}$) or amine ($-\text{NH}_2$) groups and consist of both lone-pair interactions (accompanied by lone-pair polarization)^{35,40} and hydrogen bonds. Guanidinium alters this balance and drives a tendency to increase the surface-to-bulk ratio, leading to an increased charge carrier confinement without inducing more defects on the PNC surfaces (as explained in the next section).

Our density functional theory (DFT) calculations indicate that, beyond low concentrations of GA, these cations have an energetic preference to migrate to the surface (Fig. 2d). As the concentration of GA increases, the increase in the surface-to-bulk ratio ensures the presence of enough surface sites, at which most of the GA cations can reside (Supplementary Table 1). The inference that GA can only be incorporated into the bulk of the perovskite in low concentrations is supported by the GA concentration-dependent bulk moduli (calculated via elastic constants using the ab initio stress–

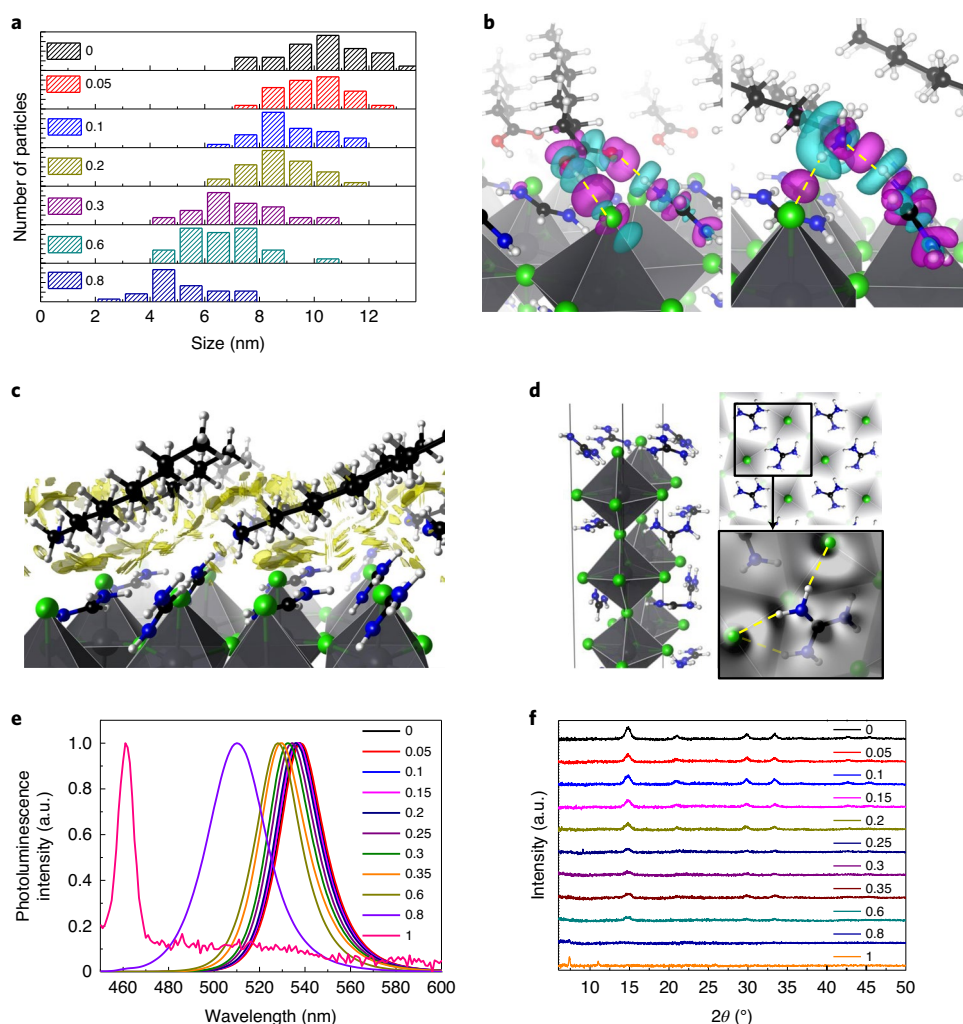


Fig. 2 | Structural and photophysical effects of GA on $\text{FA}_{1-x}\text{GA}_x\text{PbBr}_3$ PNCs. **a**, Experimentally measured size distribution of $\text{FA}_{1-x}\text{GA}_x\text{PbBr}_3$ PNCs at $0 \leq x \leq 1$. **b**, Three-dimensional charge density difference plots, showing the point chemical interactions between the perovskite surface and acid (left) or amine (right) ligands. The hydrogen and lone-pair bonds^{35,40} can be noted by the magenta lobes along the yellow dashed lines. Cyan and magenta show regions of space that are depopulated or populated by electrons, respectively (as a result of the surface-ligand bonding). **c**, Yellow regions depict dispersion interactions among the surface and surface-bound ligands. This image was generated using the Nelson complexity index (NCI; $\text{isovalue} = 0.6$)⁴². **d**, The simulated crystal structure of a GA-rich surface of $\text{FA}_{1-x}\text{GA}_x\text{PbBr}_3$ crystals is shown from the side (left) and top views (top-right). At the bottom right, a two-dimensional charge density difference plot (in greyscale)—projected on the top bromide-layer plane—shows formation of hydrogen bonds between GA and bromide (white lobes along the yellow dashed lines). **e, f**, A photoluminescence spectrum (**e**) and XRD patterns (**f**) of $\text{FA}_{1-x}\text{GA}_x\text{PbBr}_3$ PNCs at $0 \leq x \leq 1$.

strain methodology), which shows a sudden softening at higher GA concentrations (see Supplementary Fig. 4 and Supplementary Discussion 1 for more details). On the surface, the cages formed by the PbBr_6 octahedra are broken and lack a confining cap, the GA can therefore more favourably fit into the surface sites. The extra amino group can effectively stay above the surface and favourably interact with the surface bromide groups (Fig. 2d).

The photoluminescence spectrum experiments corroborate these inferences. The photoluminescence spectrum of the $\text{FA}_{0.95}\text{GA}_{0.05}\text{PbBr}_3$ PNCs (Fig. 2e, Supplementary Fig. 5a) is slightly red-shifted compared with that of FAPbBr_3 PNCs. This change confirms that small concentrations of GA incorporate into $\text{FA}_{1-x}\text{GA}_x\text{PbBr}_3$ crystals and expand the lattice. This is also confirmed by XRD patterns (Supplementary Fig. 6). As x increases (≥ 0.1), photoluminescence spectra of $\text{FA}_{1-x}\text{GA}_x\text{PbBr}_3$ gradually blue-shift while the intensity of the XRD peaks drops due to the size decrease (Fig. 2f). At $x > 0.6$, the structure of the PNCs begins to change, first

to an amorphous-like (or with low crystallinity) phase in which small core perovskite crystals are fully covered by GA and then to a non-perovskite guanidinium lead bromide phase (see the discussion below the Supplementary Table 1).

Defect suppression via GA doping. The surface GA population leads to effective defect passivation. The photoluminescence quantum efficiency (PLQE) improves from 79.7% for FAPbBr_3 to 93.3% for $\text{FA}_{0.9}\text{GA}_{0.1}\text{PbBr}_3$ PNCs (in solution) (Fig. 3a). $\text{FA}_{0.9}\text{GA}_{0.1}\text{PbBr}_3$ PNC films also show a PLQE of 92.45% even without using core-shell structures both in film and solution. Defect suppression is directly confirmed by deep-level transient spectroscopy (DLTS). Here, the device architecture includes indium tin oxide (ITO)/buffer hole-injection layer (Buf-HIL (ref. ²))/ $\text{FA}_{1-x}\text{GA}_x\text{PbBr}_3$ PNCs (here, $x = 0, 0.1$)/1,3,5-tris(*N*-phenyl benzimidazole-2-yl)benzene (TPBI)/LiF/Al (Fig. 3b). The DLTS spectrum shows a minimum at 250 K, which corresponds to a defect energy transition level of

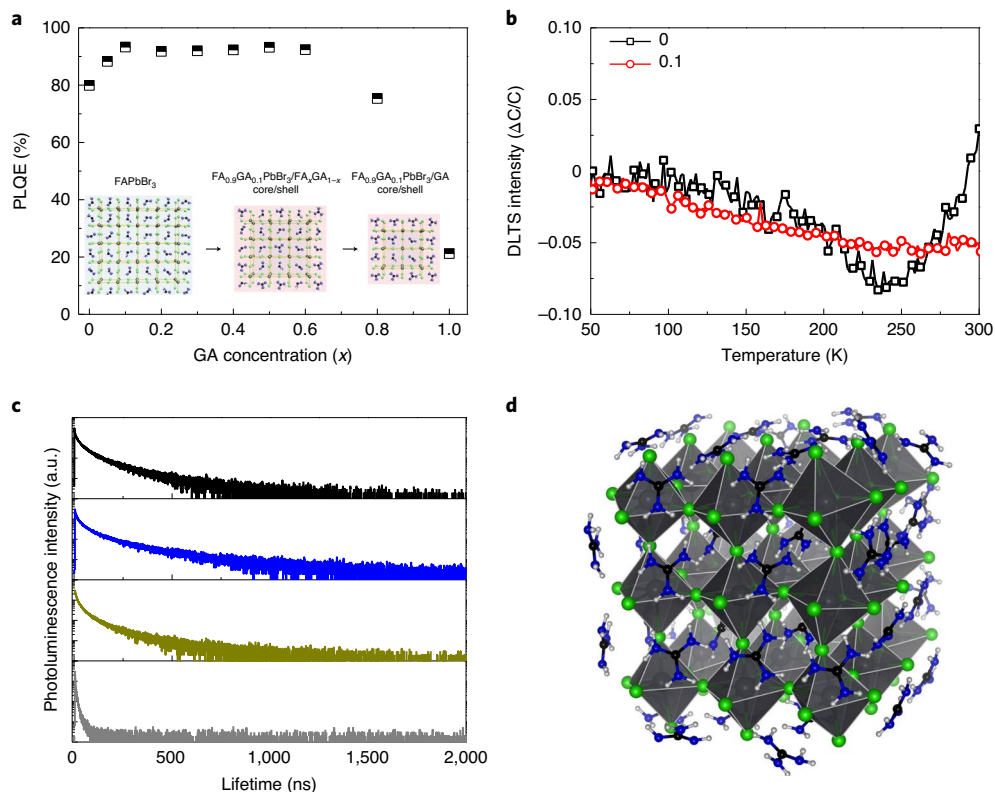


Fig. 3 | Defect analysis of $\text{FA}_{1-x}\text{GA}_x\text{PbBr}_3$ PNCs. **a**, Photoluminescence quantum efficiency and schematic crystal structures (inset) of $\text{FA}_{1-x}\text{GA}_x\text{PbBr}_3$ PNCs. **b**, Deep-level transient spectroscopy data for PeLEDs based on $\text{FA}_{1-x}\text{GA}_x\text{PbBr}_3$ PNCs at $x=0$ (black) and $x=0.1$ (red). **c**, Photoluminescence lifetimes for $\text{FA}_{1-x}\text{GA}_x\text{PbBr}_3$ PNCs at $x=0$ (black), 0.1 (blue), 0.6 (gold) and 1 (grey). **d**, A DFT-derived $\text{FA}_{1-x}\text{GA}_x\text{PbBr}_3$ quantum dot structure with a GA shell and FA core.

0.3 to 0.4 eV. This signal attenuates at $x=0.1$ and the calculated defect density N_i declines from $4.93 \times 10^{12} \text{ cm}^{-3}$ to $3.10 \times 10^{12} \text{ cm}^{-3}$ (Supplementary Table 2).

Guanidinium doping extends the photoluminescence lifetime in $\text{FA}_{0.9}\text{GA}_{0.1}\text{PbBr}_3$ (~113 ns) compared with FAPbBr_3 (~88 ns) (Fig. 3c, Supplementary Fig. 5b). Our defect suppression scheme increases: (1) the critical bias V_0 , as measured by the magnetophotocurrent in our PeLEDs (Supplementary Fig. 7a,b); (2) the thermal stability, as determined by thermogravimetric analysis (Supplementary Fig. 7c); (3) the photostability, with a smaller degree of attenuation in the shoulder of the photoluminescence spectrum peak at lower-energy states (Supplementary Fig. 7d-f); and (4) the exciton binding energy, as calculated from the temperature-dependent photoluminescence (Supplementary Fig. 7g-j and Supplementary Fig. 8).

Guanidinium stabilizes the PNC surfaces by increasing the number of hydrogen bonds (as a result of the extra amino group relative to FA) with the undercoordinated surface bromide. We have determined that the surface of the PNC has an AX termination (see Supplementary Fig. 1 and Supplementary Discussion 2). We define a cohesive energy metric for the top surface AX layer (see Supplementary Discussion 2) and use it to evaluate the increase in GA-driven surface stability. The change in this quantity (relative to no-GA surfaces) is around -350 meV (per GA) for extended surfaces (as in the basal planes of large PNCs) and around -390 meV for the very small quantum dots that we have directly modelled (Fig. 3d), due to their greater undercoordination (for example, in corners and edges) relative to extended surfaces. Here, a negative value for a change in cohesive energy means greater surface stabilization.

Density functional theory simulations of surface-binding ligands reveal relatively strong point interactions (-0.6 to -0.7 eV) with the surface (Fig. 2b), accompanied by additional

(chain-length-dependent) dispersion interactions (Fig. 2c). These interactions are the root of the surface-stabilizing effect of these ligands (see Methods for details). Guanidinium doping slightly weakens the binding of these ligands (see Supplementary Fig. 9, Supplementary Fig. 10 and the associated discussion, and the Methods); this is another indication that incorporating GA stabilizes the surface internally and decreases its reactivity toward external agents. At $x=0.1$, the PNCs are relatively large (Fig. 2a), the GA induces both bulk and surface stabilization, and is uniformly distributed. Most of the surface is still covered by FA and, due to steric hindrance, ligands can only bind to a limited number of surface sites and thus selectively bind to FA-sites, unaffected by the added GA (Supplementary Table 1). The positive effect of 10% GA is due to increased surface stability, reduced defects and increased electron-hole confinement, in addition to the bulk entropy stabilization.

By increasing the GA content and the surface-to-bulk ratio, the bulk-stabilizing effect of GA attenuates; nevertheless, as the PNC surfaces become dominantly GA terminated, its surface-stabilizing effect increases (Supplementary Table 1). Consequently, at $x=0.6$ (with a fully GA-covered surface), the PNC still showed a high PLQE of 92.4% in solutions and 91.55% in films. At $x > 0.6$, the crystallinity of the sample decreased, the perovskite phase was destabilized, new diffraction peaks appeared and the PLQE dropped (Figs. 2f and 3a). Such a departure from the perovskite structure on increasing GA content is related to the tendency of guanidinium halide perovskites to crystallize in non-perovskite structures, which was previously addressed in the literature for iodoplumbates³⁹. Our calculations also confirm this for the bromoplumbates (see Supplementary Fig. 11 and Methods for details). Our PNC materials design strategy for light-emitting diodes (LEDs) can be extended to halide perovskites with other halides and cations; to

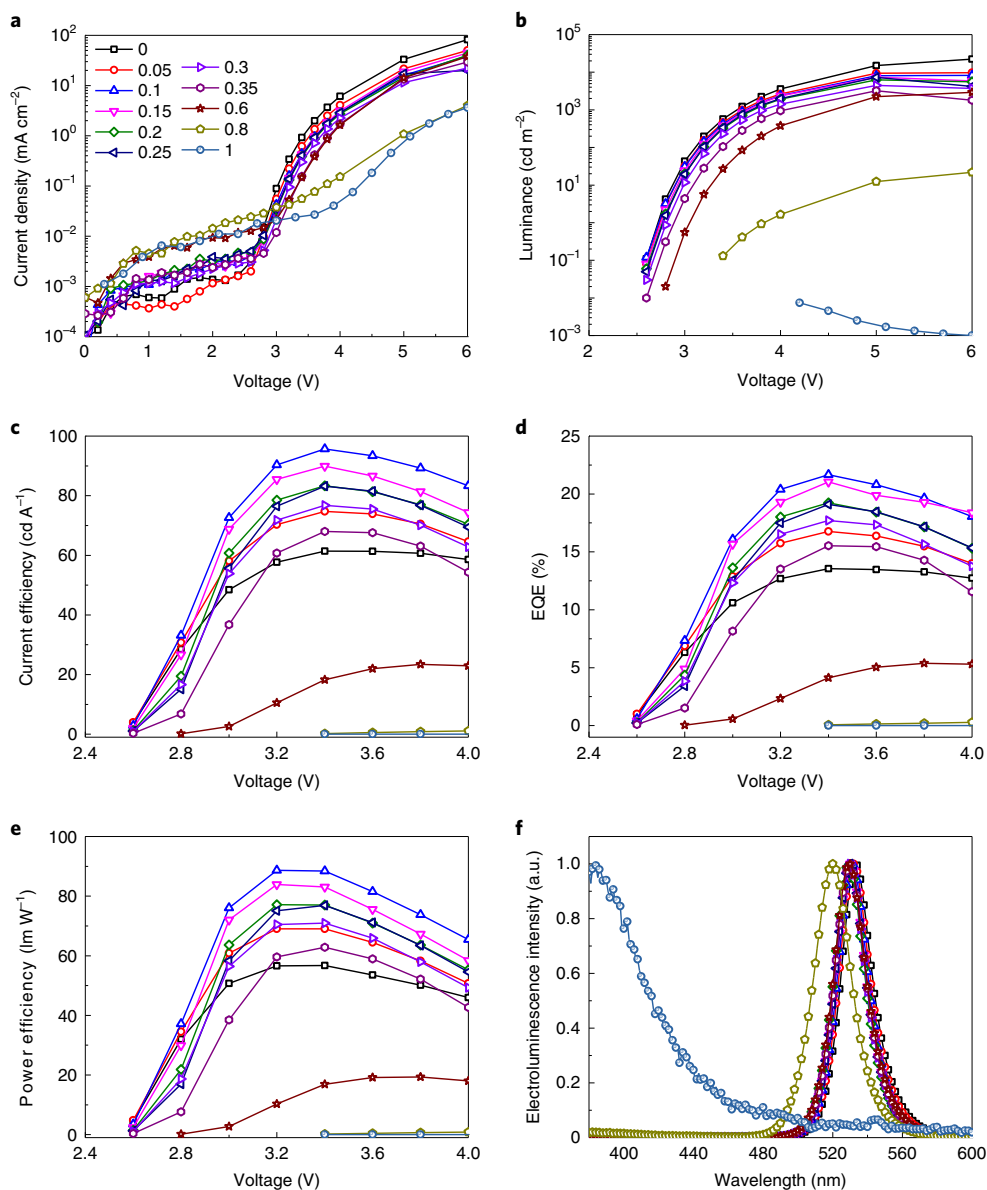


Fig. 4 | Characteristics of PeLEDs based on FA_{1-x}GA_xPbBr₃ PNCs. a–f, Current density (a), luminance (b), current efficiency (c), external quantum efficiency (d), power efficiency (e) and electroluminescence spectrum (f) of PeLEDs based on FA_{1-x}GA_xPbBr₃ PNCs (0 ≤ x ≤ 1).

showcase this, we have experimentally studied methylammonium lead bromide (MAPbBr₃) PNCs. About 10% GA can be incorporated into MAPbBr₃ crystals, inducing red-shifted photoluminescence. Beyond ~10%, GA is driven to the surface and reduces the size of the PNCs, inducing blue-shifted photoluminescence (Supplementary Fig. 12). The GA leads to effective defect passivation and improved PLQE in MAPbBr₃ PNCs. To further indicate the novel effects induced by the doped GA cations on colloidal PNCs, we experimentally studied FAPbBr₃ PNCs with other types of organic cations such as butylammonium bromide, octylammonium bromide, benzylammonium bromide and phenethylammonium bromide (Supplementary Fig. 13). As the content of these organic cations increases (>0.2), the PNCs show limited improvement in PLQE (<86%) and several different shoulder peaks in photoluminescence spectrum due to various sizes or compositions of crystals. These results indicate that GA—featuring only one extra amino group and mainly residing on the surface of the colloidal PNCs—is a well-controlled materials alloying concept. The doped

GA can suppress both the bulk and surface defects, with minimal changes to the dimensionality and composition, and can simultaneously increase the radiative recombination of the colloidal PNCs.

The use of GA to passivate the defects in MAPbI₃-based polycrystalline bulk films for solar cells has been reported^{32,33}. In our work we: (1) synthesize colloidal PNCs rather than perovskite polycrystalline bulk films, thus the GA—in addition to passivating defects—simultaneously controls the size of the PNCs and enhances radiative recombination; (2) understand why GA can be incorporated into the PNC in small concentrations (~10%), above which it migrates to the surface outermost layer of PNC; and (3) illustrate competing enthalpic and entropic effects for GA incorporation in the bulk and show that such a mixed phase is entropy stabilized.

Achieving highest LED efficiencies. The electroluminescence efficiency of our PeLEDs (structure: ITO/Buf-HIL/FA_{1-x}GA_xPbBr₃ PNCs/TPBI/LiF/Al) increased from 61.3 to 95.7 cd A⁻¹ (Fig. 4) as x increased from 0 to 0.1. As x increases above 0.1, the current densi-

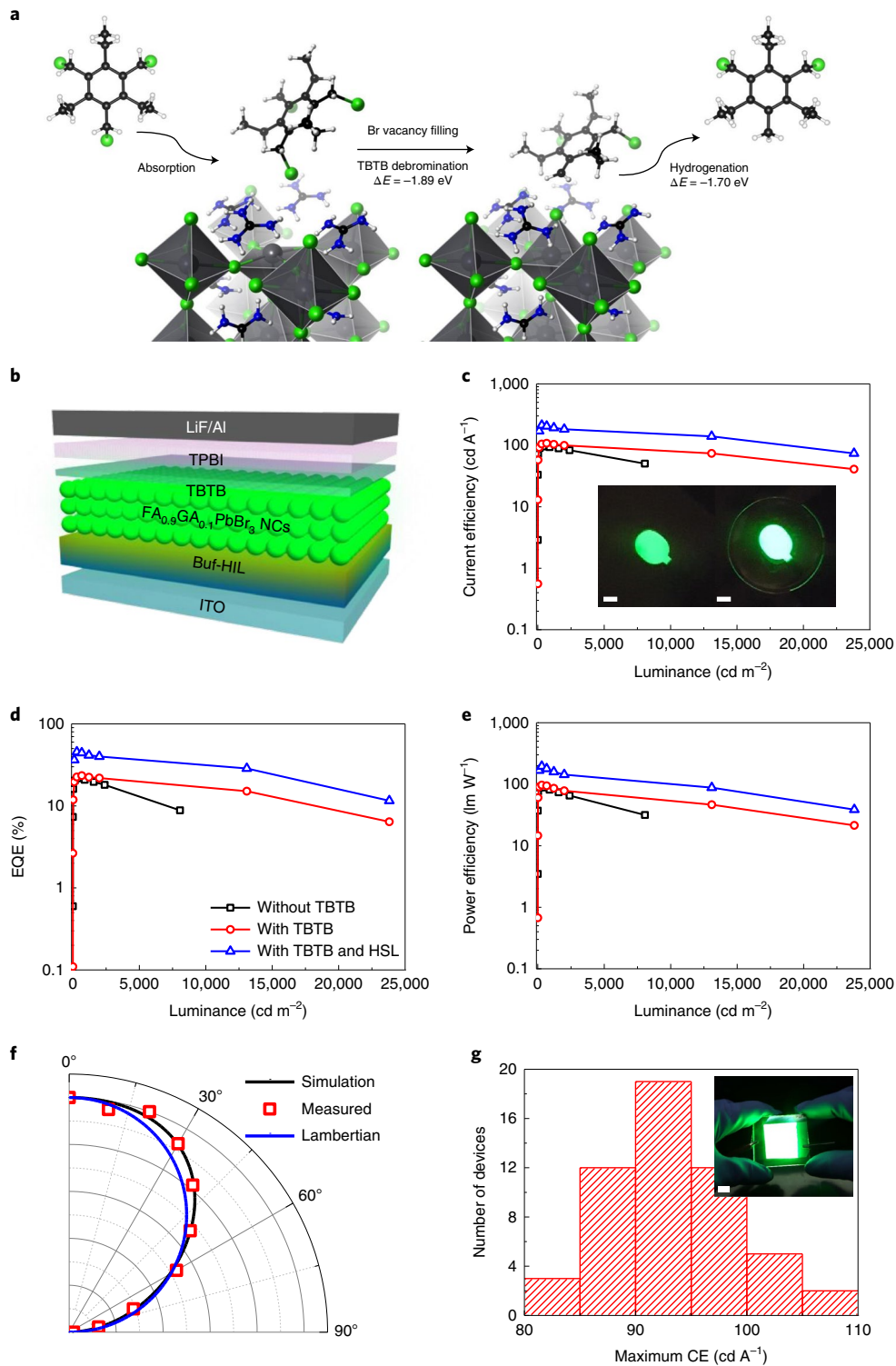


Fig. 5 | Characteristics of PeLEDs with a TBTB interlayer. a, DFT-derived mechanism for bromide vacancy healing process driven by TBTB molecules on GA-terminated FAPbBr_3 surface. The debrominated radical can then achieve greater stability via further hydrogenation. The reaction energies (negative means exothermic) are shown by ΔE . **b**, Device structure of $(x=0.1)$ PeLEDs with TBTB interlayer. **c–e**, Current efficiency (**c**), external quantum efficiency (**d**) and power efficiency (**e**) of PeLED devices ($x=0.1$) with or without a TBTB interlayer and a hemispherical lens (HSL). The insets in **c** are photographs of operating devices with TBTB, without (left) and with (right) a hemispherical lens (scale bar, 1 mm). **f**, Angular intensity profiles for simulated emission, measured electroluminescence emission and Lambertian emission according to the viewing angles. **g**, Current efficiency histogram and photograph (inset; scale bar, 1 cm) of an operating large-area PeLEDs ($3\text{ cm} \times 3\text{ cm}$ pixel) with TBTB interlayer ($x=0.1$).

ties, luminance and electroluminescence efficiencies of the PeLEDs gradually decrease; this trend can be ascribed to an increased ratio of insulating organic ligands surrounding the PNCs due to the

increased surface-to-bulk ratio (Fig. 2a). The increased number of these insulating ligands hinders charge transport to the PNCs and thereby reduces the electroluminescence efficiency⁴¹.

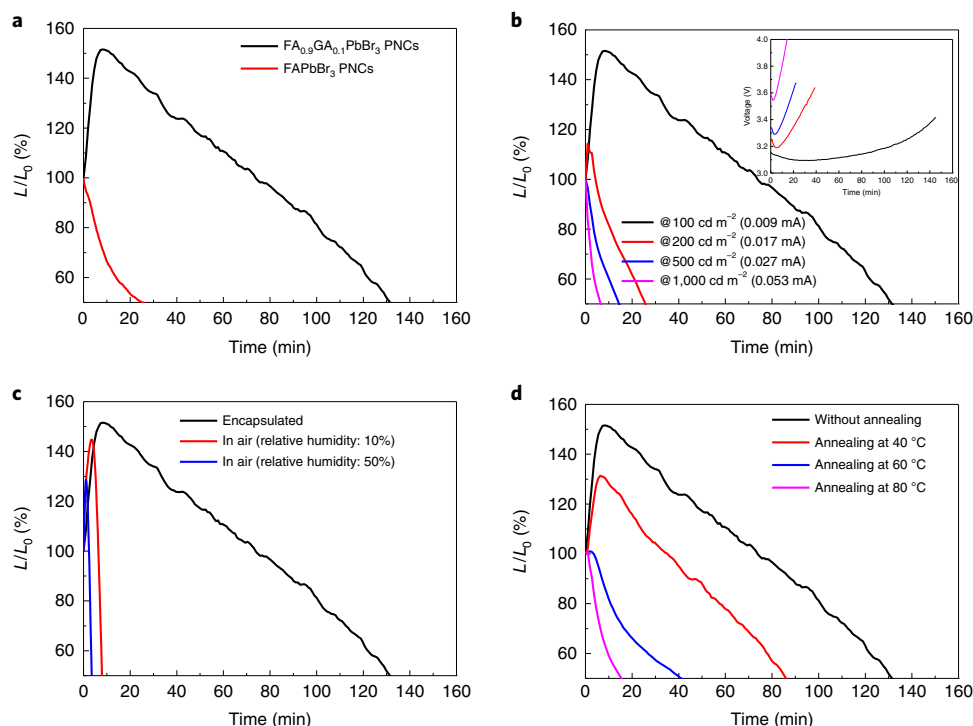


Fig. 6 | Device lifetime of PeLEDs. **a**, The device lifetimes of PeLEDs based on $\text{FA}_{0.9}\text{GA}_{0.1}\text{PbBr}_3$ PNCs and FAPbBr_3 PNCs at an initial luminance (L_0) of 100 cd m^{-2} . **b**, The device lifetimes and operating voltages (inset) of PeLEDs based on $\text{FA}_{0.9}\text{GA}_{0.1}\text{PbBr}_3$ PNCs under different initial measurement luminance (applied current). **c**, The device lifetimes of PeLEDs based on $\text{FA}_{0.9}\text{GA}_{0.1}\text{PbBr}_3$ PNCs at an initial luminance of 100 cd m^{-2} under various environmental conditions. **d**, The device lifetimes of PeLEDs based on $\text{FA}_{0.9}\text{GA}_{0.1}\text{PbBr}_3$ PNCs at an initial luminance of 100 cd m^{-2} with different thermal annealing temperatures of devices.

We extended our strategy to further suppress surface defects and minimize non-radiative recombination losses in the $\text{FA}_{0.9}\text{GA}_{0.1}\text{PbBr}_3$ PNC films by introducing TBTB interlayers ($\sim 5 \text{ nm}$) between the PNC films and the TPBI layers, which can act as a bromide vacancy healing agent and suppress surface defects in the PNC films. As can be seen in Fig. 5a, a TBTB molecule can readily deposit its bromine into a surface bromide vacancy. The debrominated radical can then become hydrogenated in the environment containing acid ligands surrounding the PNCs and gets further stabilized (see Supplementary Discussion 2 for more details). These defect healing effects are confirmed by a decreased defect peak intensity and N_1 in the DLTS measurements, by an increased photoluminescence lifetime, and by a blue-shifted photoluminescence spectrum (Supplementary Fig. 14a–c, Table 2). The insulating TBTB interlayers on the PNC films can also improve the charge balance in PeLEDs by retarding electron injection into emitting layers. This is confirmed by measuring the electron current densities in electron-only devices (ITO/polyethylenimine ethoxylated (10 nm)/ $\text{FA}_{0.9}\text{GA}_{0.1}\text{PbBr}_3$ PNCs with or without TBTB/TPBI/LiF/Al), by measuring hole current densities in hole-only devices (ITO/Buf-HIL/ $\text{FA}_{0.9}\text{GA}_{0.1}\text{PbBr}_3$ PNC films with or without TBTB/Tris(4-carbazoyl-9-ylphenyl)amine (50 nm)/ MoO_3/Al) (Supplementary Fig. 14d,e). Furthermore, capacitance–voltage characteristics in PeLEDs corroborate the delay in electron injection on inserting the TBTB interlayer (Supplementary Fig. 14f). PeLEDs based on $\text{FA}_{0.9}\text{GA}_{0.1}\text{PbBr}_3$ PNCs and TBTB interlayers reach a maximum current efficiency of 108 cd A^{-1} and an EQE = 23.4%, calculated by using the full angular electroluminescence distribution (Fig. 5b–f). The distribution of current efficiency obtained among 53 devices shows great reproducibility (Fig. 5g). We further improve the efficiency of our PeLEDs (to current efficiency = 203 cd A^{-1} and EQE = 45.5%) by placing a light outcoupling hemispherical lens on the emitting glass substrate. Optical simulations also verify that our

devices—without and with an outcoupling hemispherical lens—can reach EQEs of 30.2% and 55.61%, respectively (provided that the PLQE of PNC films is ~ 1 and absorption loss of the emitting layer is negligible) (Supplementary Fig. 15). These are the highest efficiencies so far reported among PeLEDs based on either polycrystalline bulk films or PNCs and surpass even the highest current efficiency of conventional III–V and II–VI inorganic quantum dot LEDs (Supplementary Fig. 16 and Supplementary Tables 3 and 4). We also fabricated large-area PeLEDs ($3 \text{ cm} \times 3 \text{ cm}$ pixel) that used $\text{FA}_{0.9}\text{GA}_{0.1}\text{PbBr}_3$ PNCs (Fig. 5g inset) to demonstrate the promise of using organic–inorganic hybrid colloidal PNCs in solid-state lighting devices and displays. Device lifetime of our PeLEDs were measured under various operational and environmental conditions (Fig. 6, Supplementary Fig. 17). PeLEDs based on $\text{FA}_{0.9}\text{GA}_{0.1}\text{PbBr}_3$ PNCs and TBTB interlayers showed a lifetime (when the initial luminance drops to 50%) of 132 min with an initial luminance of 100 cd m^{-2} , which is improved by a factor of ~ 5.3 relative to PeLEDs based on FAPbBr_3 PNCs (lifetime = 25 min) and ~ 8 relative to the previously reported highest-efficiency PeLEDs based on FAPbBr_3 PNCs (lifetime = 18 min)²⁴.

Conclusions

We developed a comprehensive strategy that leads to a considerable increase in the luminescence efficiency of PNCs. This strategy makes it possible to simultaneously (1) decrease the non-radiative charge recombination by comprehensive defect suppression and bulk entropy stabilization and (2) increase the radiative recombination of charge carriers due to increased excitonic confinement. First, we used substitutional doping of GA into FAPbBr_3 PNCs to incorporate an optimal proportion of GA cations into the structure. The GA cations can reside in the bulk of the PNC in low concentrations ($\sim 10\%$). The surplus GA then accumulates on the surface

of the PNC. Guanidinium incorporation provides bulk entropy stabilization, surface stabilization (by additional hydrogen bonding contributed by their extra amino group), and better electron–hole confinement. A GA to FA ratio of 0.1 was shown to maximize the electroluminescence efficiency. Moreover, a TBTB overcoat was introduced to heal the halide vacancy defects in $\text{FA}_{1-x}\text{GA}_x\text{PbBr}_3$ PNCs and to improve the charge balance in PeLEDs. These synergistic strategies yielded the highest electroluminescence efficiencies in PNC-based PeLEDs ($\text{CE} = 108 \text{ cd A}^{-1}$ and $\text{EQE} = 23.4\%$; $\text{CE} = 203 \text{ cd A}^{-1}$ and $\text{EQE} = 45.5\%$ with hemispherical lens). Our efficiencies demonstrate that this design strategy provides a clear pathway to translate PNCs into PeLEDs for a new generation of high-efficiency display applications.

Online content

Any methods, additional references, Nature Research reporting summaries, source data, extended data, supplementary information, acknowledgements, peer review information; details of author contributions and competing interests; and statements of data and code availability are available at <https://doi.org/10.1038/s41566-020-00732-4>.

Received: 1 February 2020; Accepted: 28 October 2020;

Published online: 04 January 2021

References

1. Tan, Z.-K. et al. Bright light-emitting diodes based on organometal halide perovskite. *Nat. Nanotechnol.* **9**, 687–692 (2014).
2. Kim, Y.-H. et al. Multicolored organic/inorganic hybrid perovskite light-emitting diodes. *Adv. Mater.* **27**, 1248–1254 (2015).
3. Cho, H. et al. Overcoming the electroluminescence efficiency limitations of perovskite light-emitting diodes. *Science* **350**, 1222–1225 (2015).
4. Protesescu, L. et al. Nanocrystals of cesium lead halide perovskites (CsPbX_3 , X = Cl, Br, and I): novel optoelectronic materials showing bright emission with wide color gamut. *Nano Lett.* **15**, 3692–3696 (2015).
5. Schmidt, L. C. et al. Nontemplate synthesis of $\text{CH}_3\text{NH}_3\text{PbBr}_3$ perovskite nanoparticles. *J. Am. Chem. Soc.* **136**, 850–853 (2014).
6. Kim, Y.-H., Cho, H. & Lee, T.-W. Metal halide perovskite light emitters. *Proc. Natl Acad. Sci. USA* **113**, 11694–11702 (2016).
7. Kim, Y.-H., Kim, J. S. & Lee, T.-W. Strategies to improve luminescence efficiency of metal-halide perovskites and light-emitting diodes. *Adv. Mater.* **31**, 1804595 (2019).
8. Koscher, B. A., Swabeck, J. K., Bronstein, N. D. & Alivisatos, A. P. Essentially trap-free CsPbBr_3 colloidal nanocrystals by postsynthetic thiocyanate surface treatment. *J. Am. Chem. Soc.* **139**, 6566–6569 (2017).
9. De Roo, J. et al. Highly dynamic ligand binding and light absorption coefficient of cesium lead bromide perovskite nanocrystals. *ACS Nano* **10**, 2071–2081 (2016).
10. Wang, H.-C. et al. High-performance $\text{CsPb}_{1-x}\text{Sn}_x\text{Br}_3$ perovskite quantum dots for light-emitting diodes. *Angew. Chem. Int. Ed.* **129**, 13838–13842 (2017).
11. Chiba, T. et al. Anion-exchange red perovskite quantum dots with ammonium iodine salts for highly efficient light-emitting devices. *Nat. Photon.* **12**, 681–687 (2018).
12. Song, J. et al. Organic–inorganic hybrid passivation enables perovskite QLEDs with an EQE of 16.48%. *Adv. Mater.* **30**, 1805409 (2018).
13. Park, M.-H. et al. Boosting efficiency in polycrystalline metal halide perovskite light-emitting diodes. *ACS Energy Lett.* **4**, 1134–1149 (2019).
14. Xu, W. et al. Rational molecular passivation for high-performance perovskite light-emitting diodes. *Nat. Photon.* **13**, 418–424 (2019).
15. Zhao, X. & Tan, Z.-K. Large-area near-infrared perovskite light-emitting diodes. *Nat. Photon.* **14**, 215–218 (2020).
16. Yang, Y. et al. Comparison of recombination dynamics in $\text{CH}_3\text{NH}_3\text{PbBr}_3$ and $\text{CH}_3\text{NH}_3\text{PbI}_3$ perovskite films: influence of exciton binding energy. *J. Phys. Chem. Lett.* **6**, 4688–4692 (2015).
17. Stranks, S. D. et al. Recombination kinetics in organic–inorganic perovskites: excitons, free charge, and subgap states. *Phys. Rev. Appl.* **2**, 034007 (2014).
18. Lin, K. et al. Perovskite light-emitting diodes with external quantum efficiency exceeding 20 per cent. *Nature* **562**, 245–248 (2018).
19. Xiao, Z. et al. Efficient perovskite light-emitting diodes featuring nanometre-sized crystallites. *Nat. Photon.* **11**, 108–115 (2017).
20. Zhao, B. et al. High-efficiency perovskite–polymer bulk heterostructure light-emitting diodes. *Nat. Photon.* **12**, 783–789 (2018).
21. Cao, Y. et al. Perovskite light-emitting diodes based on spontaneously formed submicrometre-scale structures. *Nature* **562**, 249–253 (2018).
22. Yang, X. et al. Efficient green light-emitting diodes based on quasi-two-dimensional composition and phase engineered perovskite with surface passivation. *Nat. Commun.* **9**, 570 (2018).
23. Zhao, L. et al. Electrical stress influences the efficiency of $\text{CH}_3\text{NH}_3\text{PbI}_3$ perovskite light emitting devices. *Adv. Mater.* **29**, 1605317 (2017).
24. Chen, H. et al. High-efficiency formamidinium lead bromide perovskite nanocrystal-based light-emitting diodes fabricated via a surface defect self-passivation strategy. *Adv. Opt. Mater.* **8**, 1901390 (2020).
25. Zhu, H. et al. Screening in crystalline liquids protects energetic carriers in hybrid perovskites. *Science* **353**, 1409–1413 (2016).
26. Yang, Y. et al. Observation of a hot-phonon bottleneck in lead-iodide perovskites. *Nat. Photon.* **10**, 53–59 (2016).
27. Zheng, F., Tan, L. Z., Liu, S. & Rappe, A. M. Rashba spin–orbit coupling enhanced carrier lifetime in $\text{CH}_3\text{NH}_3\text{PbI}_3$. *Nano Lett.* **15**, 7794–7800 (2015).
28. Rappe, A. M., Grinberg, I. & Spanier, J. E. Getting a charge out of hybrid perovskites. *Proc. Natl Acad. Sci. USA* **114**, 7191–7193 (2017).
29. Swarnkar, A. et al. Quantum dot-induced phase stabilization of $\alpha\text{-CsPbI}_3$ perovskite for high-efficiency photovoltaics. *Science* **354**, 92–95 (2016).
30. Banerjee, A., Chakraborty, S. & Ahuja, R. Bromination-induced stability enhancement with a multivalley optical response signature in guanidinium $[\text{C}(\text{NH}_2)_3]^+$ -based hybrid perovskite solar cells. *J. Mater. Chem. A* **5**, 18561–18568 (2017).
31. Giorgi, G., Fujisawa, J.-I., Segawa, H. & Yamashita, K. Organic–inorganic hybrid lead iodide perovskite featuring zero dipole moment guanidinium cations: a theoretical analysis. *J. Phys. Chem. C* **119**, 4694–4701 (2015).
32. Jodlowski, A. D. et al. Large guanidinium cation mixed with methylammonium in lead iodide perovskites for 19% efficient solar cells. *Nat. Energy* **2**, 972–979 (2017).
33. Marco, N. D. et al. Guanidinium: a route to enhanced carrier lifetime and open-circuit voltage in hybrid perovskite solar cells. *Nano Lett.* **16**, 1009–1016 (2016).
34. Kanno, S., Imamura, Y. & Hada, M. First-principles calculations of the rotational motion and hydrogen bond capability of large organic cations in hybrid perovskites. *J. Phys. Chem. C* **122**, 15966–15972 (2018).
35. Kakekhani, A., Katti, R. N. & Rappe, A. M. Water in hybrid perovskites: bulk MAPbI₃ degradation via super-hydrous state. *APL Mater.* **7**, 041112 (2019).
36. Yi, C. et al. Entropic stabilization of mixed A-cation ABX_3 metal halide perovskites for high performance perovskite solar cells. *Energy Environ. Sci.* **9**, 656–662 (2016).
37. Travis, W., Glover, E. N. K., Bronstein, H., Scanlon, D. O. & Palgrave, R. G. On the application of the tolerance factor to inorganic and hybrid halide perovskites: a revised system. *Chem. Sci.* **7**, 4548–4556 (2016).
38. Pham, N. D. et al. Tailoring crystal structure of $\text{FA}_{0.83}\text{Cs}_{0.17}\text{PbI}_3$ perovskite through guanidinium doping for enhanced performance and tunable hysteresis of planar perovskite solar cells. *Adv. Funct. Mater.* **29**, 1806479 (2019).
39. Deng, Z., Kieslich, G., Bristowe, P. D., Cheetham, A. K. & Sun, S. Octahedral connectivity and its role in determining the phase stabilities and electronic structures of low-dimensional, perovskite-related iodoplumbates. *APL Mater.* **6**, 114202 (2018).
40. Kakekhani, A. et al. Nature of lone-pair–surface bonds and their scaling relations. *Inorg. Chem.* **57**, 7222–7238 (2018).
41. Kim, Y.-H. et al. Highly efficient light-emitting diodes of colloidal metal-halide perovskite nanocrystals beyond quantum size. *ACS Nano* **11**, 6586–6593 (2017).
42. Contreras-Garcia, J. et al. NCIPLOT: a program for plotting noncovalent interaction regions. *J. Chem. Theory Comput.* **7**, 625–632 (2011).

Publisher's note Springer Nature remains neutral with regard to jurisdictional claims in published maps and institutional affiliations.

© The Author(s), under exclusive licence to Springer Nature Limited 2021

Methods

Synthesis of PNCs. All $\text{FA}_{1-x}\text{GA}_x\text{PbBr}_3$ PNCs were synthesized in air at room temperature. Precursor solutions were prepared by dissolving FABr (Dyesol), GABr (Dyesol) and PbBr_2 (Aldrich, 99.999%), with the FABr:GABr ratio changing from 1:0 to 0:1 while maintaining the molarity of FABr:GABr at 0.1 mmol and the molarity of PbBr_2 at 0.2 mmol, in 0.5 ml of anhydrous N,N -dimethylformamide (Aldrich, 99.8%); 0.15 ml of precursor solution was then dropped into a crystallization-inducing solution comprising 5 ml of toluene, 2 ml of 1-butanol, 0.3 ml of oleic acid and 24.2 μl of *n*-decylamine, which was mixed for 10 min under vigorous stirring. The resulting colloidal PNCs were washed by sequential centrifugation and then collected in toluene.

PeLED fabrication. Indium tin oxide patterned glasses were cleaned by sequential sonication in acetone and 2-isopropanol for 15 min each. The glasses were boiled in 2-isopropanol for 20 min, then transferred into an ultraviolet-ozone cleaner and treated with ultraviolet-ozone for 10 min to remove the residual organics. Buf-HILS composed of poly(3,4-ethylenedioxythiophene)/poly(styrene sulfonate) and perfluorinated ionomer were then spin-coated in air to make a 40-nm-thick layer, which was then annealed at 150 °C for 30 min. The samples were then transferred into a glove box, in which emitting layers were formed by spin-coating appropriate $\text{FA}_{1-x}\text{GA}_x\text{PbBr}_3$ PNC solutions at 1,000 r.p.m. for 60 s. To fabricate the 5-nm-thick TBTB layer, TBTB solutions, which were dissolved in toluene, were spincoated at 3,000 r.p.m. for 60 sec. The samples were transferred to a vacuum evaporator, and then a 50-nm-thick layer of TPBI, a 1-nm-thick layer of LiF and a 100-nm-thick layer of aluminium were sequentially deposited.

General information on our DFT simulations. We performed DFT calculations with plane-wave basis sets using the Quantum Espresso software package⁴³. Ultrasoft GBRV pseudopotentials⁴⁴ and Perdew–Burke–Ernzerhof exchange correlations were used⁴⁵. Dispersion interactions were accounted for using the Grimme DFT-D3 method⁴⁶. The inclusion of dispersion interactions to accurately describe hybrid perovskite systems has been shown to be important⁴⁷. As mentioned in the main text (in the context of Fig. 1c), the DFT-D3 dispersion correction can accurately describe the experimental data. We used a k-mesh sampling density greater than 15,000 points per \AA^3 . The plane-wave energy cutoff (E_{cut}) was set to ~ 550 eV, whereas the charge cutoff was set to ten times this value. We set the force convergence criteria for the relaxation calculations as very small: each force component on each atom needed to be smaller than 10^{-4} Rydberg per Bohr radius. Relative to the regular solid-state structures, we have molecular groups as part of the structure; consequently, the energy landscape can have regions with very small energy gradients (mostly corresponding to the rotations of the molecular groups), thus precise calculations of forces and low enough force convergence thresholds were necessary to properly explore the real local minima of such structures. Most of our calculations (except some molecule-in-box calculations) were variable-cell relaxations (vc-relax), in which both the atomic coordinates and the cell vectors were optimized to find the zero-force, zero-stress structures with minimum internal energy. The smearing scheme for the occupations of the Kohn–Sham orbitals was the cold smearing of Marzari and Vanderbilt⁴⁸, with a temperature equal to $10 \text{ mRy}/k_{\text{B}}$ (where k_{B} is the Boltzmann constant). The computational XRD patterns were generated using the Mercury software⁴⁹, with fully relaxed atomic coordinates and lattice constants as input. Using the aforementioned convergence parameters, we successfully achieved the precision (~ 1 meV per formula unit cell (f.u.c.)) we needed in formation energy plots (Fig. 1d), and a virtually perfect structural agreement with the experiment (Fig. 1c). We used norm-conserving pseudopotentials—as opposed to ultrasoft ones—to calculate the reduced density gradient and the NCI index⁴²; E_{cut} was set to ~ 680 eV for these calculations. The charge density differences calculations for the binding of ligands were also performed using norm-conserving pseudopotentials to be consistent with the NCI plots.

Photoluminescence and PLQE measurement. Photoluminescence spectra of $\text{FA}_{1-x}\text{GA}_x\text{PbBr}_3$ PNCs in solution states were measured using a JASCO FP8500 spectrofluorometer. Photoluminescence quantum efficiencies were detected using a 100 nm integrating sphere (ILF-835) that was mounted on the same spectrofluorometer, and calculated using JASCO SpectraManager II Software. The PLQE of the thin film samples was measured using an integrating sphere method. A continuous-wave 405 nm blue diode laser with an excitation power of 50 μW and a focused beam spot of $\sim 0.3 \text{ mm}^2$ was used to photoexcite the samples. Emission was measured using an Andor iDus Silicon detector. The samples were encapsulated between two glass cover slips before measurements.

Time-correlated single-photon counting measurement. Photoluminescence lifetimes of $\text{FA}_{1-x}\text{GA}_x\text{PbBr}_3$ PNCs were measured using a FluoTime 300. $\text{FA}_{1-x}\text{GA}_x\text{PbBr}_3$ PNCs were photoexcited by a picosecond-pulse laser head (excitation wavelength = 405 nm, LDH-P-C-405B, PicoQuant) and their photoluminescence lifetimes were detected using a photon counting detector (PMA Hybrid 07) and a time-correlated single-photon counting measurement module (PicoHarp, PicoQuant).

Transmission electron microscopy measurement. To measure the transmission electron microscopy images of the PNCs, 0.05 ml of $\text{FA}_{1-x}\text{GA}_x\text{PbBr}_3$ PNC solutions were dropped onto a copper grid and measured using a JEOL-JEM 2100F with an acceleration voltage of 200 kV.

DLTS. Deep-level transient spectroscopy measurements were performed with a PhysTech FT1030 DLTS system. The capacitance was measured using a modified Boonton 72B capacitance meter with a 1 MHz. Temperature scans were performed between 20 and 300 K at a heating rate of 2 K min^{-1} . Samples were placed in the helium-contact gas of a liquid helium cryostat. The pulse height, filling pulse width and pulse period width were 0.4 V, 10 ms and 10 ms, respectively. The activation energy, capture cross-section and concentration of traps were calculated using an Arrhenius plot.

DFT calculations of structures. We used a fully vc-relaxed, self-consistent DFT-derived structure to model the hybrid perovskite systems we have studied in this work. This means no constraint was assumed and implemented on the atomic positions or lattice vectors. In hybrid perovskite materials, the higher temperatures derive the structures towards higher effective symmetries due to thermal and spatial averaging of the local structural symmetries. The nominal higher symmetry (cubic) perovskite structures deduced from XRD, which are macroscopically averaged, should not be used to model the electronic properties (naturally including formation and binding energies), which are sensitive to the order and coordination of atoms in angstrom scale rather than a macroscopic average. FAPbBr₃ is experimentally known to have a low temperature orthorhombic structure and a room temperature cubic phase. Both of these are actually an averaged order and we find a (technically speaking) triclinic structure to be the fully self-consistent DFT structure. This structure is greatly similar to the orthorhombic phase (only very small deviations in cell parameters from the ideal orthorhombic phase) and is depicted in Fig. 1b. The volume of such a structure is $\sim 852 \text{ \AA}^3$, which was within $\sim 2\%$ error of the experimentally measured value for this phase. This corresponds to an error of $\sim 0.5\%$ in lattice constants. Moreover, as mentioned in the main text, such a structure was able to reproduce the experimental XRD patterns virtually perfectly (Fig. 1c). As has been pointed out experimentally, such a phase has a $c(2 \times 2) \times 2$ structure, in which the FA cations have an alternative orientational pattern, that is, the long direction of the molecule alternates its orientation (Fig. 1c). We also perform DFT calculations of surfaces and quantum dots (see Supplementary Discussion 2 for more details).

DFT calculations of bulk energies. We perform the procedure explained below to calculate the internal and free energies reported in Fig. 1d. For calculations regarding 0, 25, 50, 75 and 100% GA content, we use the $c(2 \times 2) \times 2$ structure that was previously mentioned. We dope the aforementioned structure with the needed GA, make a number of initial guesses and then fully vc-relax the structures with no constraints. For 12.5% concentration, we use a $2 \times 2 \times 2$ supercell. The relative internal energies reported in Fig. 1d are relative to the precursors, and the 0 has been chosen to be that of FAPbBr₃. The precursors are DFT-derived PbBr_2 , GABr and FABr. The free energy was derived by adding the configurational entropy and (zero-temperature DFT-derived) internal energy contributions. The configurational entropy (per f.u.c. for $\text{FA}_{1-x}\text{GA}_x\text{PbBr}_3$) was calculated using the analytic formula for ideal alloys, which has been shown to be an effective model for entropy stabilization of hybrid perovskite systems: $S = k_{\text{B}}[\ln x + (1-x)\ln(1-x)]$ ³⁶.

DFT calculations of acid or amine binding energies. An important part of our experiments was the stabilizing role of the long-chain acids and amines we synthesize our PNCs in. Specifically, we use oleic acid and decylamine. We performed DFT calculations to understand how such ligands bind to our PNC's surfaces and how and what extent they stabilize these surfaces. Our calculations indicate that our perovskite samples possess an AX-termination (see Supplementary Section 2 for more details). Consequently, we study the interaction of acids and bases to such surfaces, and we investigate how the presence of surface GA groups changes the binding.

We performed a set of numerical experiments to understand the interaction between the ligands and the surface. We study the binding energy of the acid and amines as a function of their chain length (Supplementary Fig. 9). The surface binding energy of the ligand was sizable and was in the root of their stabilizing effect on our PNCs. The amines interact via their nitrogen $2p$ lone-pair orbital, with the proton-like nitrogen-bound hydrogen of the surface organic cation, while an amine hydrogen forms a hydrogen bond with the surface bromide (Fig. 2b). The acid interacts from the oxygen end with the proton-like nitrogen-bound hydrogen of the surface organic cation, whereas the acid OH group interacts via its hydrogen with the surface bromide (Fig. 2b). It can be seen that the interaction between the acids and amines can be decomposed into two parts: (1) a strong point interaction that is present for smaller-chain acids and amines, (2) a weaker non-local van der Waals interaction (Fig. 2c) that is a function of the chain length, the folding of the chain relative to the surface and to the neighbouring ligands. The non-local part of the interaction closely depends on the specific orientation and folding of the ligand relative to the surface and neighbouring ligands, which is naturally affected by the thermal motions and steric hindrance. Nevertheless, the

property we were more interested in was the change in the ligand binding upon GA doping. Such a quantity is more robust and less dependent on the non-local part of the interaction, as the change in surface cation (FA to GA) mostly changes the local part of the interaction. Consequently, we quantify the change in the binding energy by introducing the GA via investigating the binding of short-chain acids and amines (acetic acid and ethylamine), which are dominated by the local point interactions (Supplementary Fig. 9a). Probing the trends in adsorption energies of some adsorbates, using smaller adsorbates with identical chemical groups interacting with the surface, is similar in philosophy to the idea of scaling relations in surface chemistry and catalysis. As mentioned in the main text, the GA doping slightly weakens the binding of these ligands (Supplementary Fig. 9b,c); this result was yet another indication that incorporating GA stabilizes the surface internally and decreases its reactivity toward external agents.

As a side note, the data used for Supplementary Fig. 9a to decompose the interaction of acids and amines as well as Figs. 2b and 2c, have been generated based on an earlier set of calculations performed with a slightly higher energy bulk structure with an effective $1 \times 1 \times 1$ reconstruction for FAPbBr_3 , as opposed to $c(2 \times 2) \times 2$. Nevertheless, the conclusions of these figures are robust, as we extract the trends among binding energies and the nature of chemical bonds, as opposed to absolute value of binding energies. Even the absolute values vary insignificantly when compared with the numbers that correspond to the ground-state $c(2 \times 2) \times 2$ reconstruction of the bulk FAPbBr_3 . For example, the binding energies for acetic acid and ethylamine change by 0.02 eV, which do not change the conclusions reached on the trend of binding energies in Supplementary Fig. 9a.

Perovskite phase instability of GAPbBr_3 . As mentioned in the main text, in the context of Fig. 1d, the perovskite phase of GAPbBr_3 (with 3D connectivity and corner-sharing structure) was destabilized due to the large size of GA, which was beyond the tolerance of the perovskite structure. The phase transition of GAPb_3 to an edge-sharing phase has been experimentally observed and theoretically verified in a recent work. Both our DFT and experimental results also confirm that the perovskite structure is not a relevant phase for guanidinium lead bromide. Our DFT results show that a one-dimensional edge-sharing phase for GAPbBr_3 (Supplementary Fig. 11c), was enthalpically favoured over the three-dimensional perovskite phase by -0.11 eV per f.u.c. Furthermore, as shown in Supplementary Fig. 4, the edge-sharing structure was even softer than the perovskite and thus was more entropically favoured. Consequently, the one-dimensional edge-sharing structure should possess a lower free energy than the three-dimensional perovskite structure. Density functional theory calculations show that the face-sharing phase does not have the enthalpy drive and was almost equal in internal energy to the perovskite phase. Moreover, one should note that our experimentally synthesized guanidinium lead bromide PNCs do not have to be in GAPbBr_3 stoichiometry. Another possibly relevant phase (as shown for the case of iodoplumbates) can be the GA-rich corner-sharing two-dimensional GA_xPbBr_3 structure (Supplementary Fig. 11b). Our experimental XRD patterns also confirm the deviation of the guanidinium lead bromide PNCs ($x=1$) from the perovskite structure (Supplementary Fig. 11d). Although we have not been able to theoretically match the exact phase of guanidinium lead bromide (Supplementary Fig. 11e), it was clear that, unlike lower values of x , the structure was no longer in the corner-sharing perovskite phase.

Characterization and optical simulation of PeLEDs. Electroluminescence efficiencies of the fabricated PeLEDs were measured using a Keithley 236 source measurement unit and a Minolta CS 2000 spectroradiometer. External quantum efficiency of PeLEDs was calculated by measuring full angular electroluminescence distribution⁵⁰. In analysing PeLEDs, the normalized power spectral densities were calculated using custom MATLAB codes based on the classical oscillating dipole approach. To separate the outcoupling effect, the internal quantum efficiency was set to unity. As absorption loss of the emission layer (EML) was negligible in the emission spectra, lossless EML was assumed in the simulation for numerical stability. The refractive indices of aluminium, TPBi, EML ($=\text{FA}_{0.9}\text{GA}_{0.1}\text{PbBr}_3$), BuF-HIL, ITO and glass used in the simulation were measured using spectroscopic ellipsometry (Woollam M2000D). For the refractive indices of TBTB layer, the refractive index of TPBi was applied because of its thin thickness (~ 5 nm). The emission zone was set to be located at the centre of EML, which was supported by the electron/hole-only device experiments.

Data availability

The data that support the plots within this paper and other findings of this study are available from the corresponding author on reasonable request.

References

- Giannozzi, P. et al. QUANTUM ESPRESSO: a modular and open-source software project for quantum simulations of materials. *J. Phys. Condens. Matter* **21**, 395502 (2009).
- Garrity, K. F., Bennett, J. W., Rabe, K. M. & Vanderbilt, D. Pseudopotentials for high-throughput DFT calculations. *Comput. Mater. Sci.* **81**, 446–452 (2014).
- Perdew, J. P., Burke, K. & Ernzerhof, M. Generalized gradient approximation made simple. *Phys. Rev. Lett.* **77**, 3865–3868 (1996).
- Grimme, S., Antony, J., Ehrlich, S. & Krieg, H. A consistent and accurate ab initio parametrization of density functional dispersion correction (DFT-D) for the 94 elements H–Pu. *J. Chem. Phys.* **132**, 154104 (2010).
- Wang, Y. et al. Density functional theory analysis of structural and electronic properties of orthorhombic perovskite $\text{CH}_3\text{NH}_3\text{PbI}_3$. *Phys. Chem. Chem. Phys.* **16**, 1424–1429 (2014).
- Marzari, N., Vanderbilt, D., De Vita, A. & Payne, M. C. Thermal contraction and disordering of the Al(110) surface. *Phys. Rev. Lett.* **82**, 3296–3299 (1999).
- Macrae, C. F. et al. Mercury CSD 2.0—new features for the visualization and investigation of crystal structures. *J. Appl. Cryst.* **41**, 466–470 (2008).
- Jeong, S.-H. et al. Characterizing the efficiency of perovskite solar cells and light-emitting diodes. *Joule* **4**, 1206–1235 (2020).

Acknowledgements

This work was supported by the National Research Foundation of Korea (NRF) grant funded by the Korea government (MSIT) (NRF-2016R1A3B1908431). A.K., R.B.W., and A.M.R. acknowledge the support of the US Department of Energy, Office of Basic Energy Sciences, under grant no. DE-SC0019281 and also the computational support from NERSC of the DOE. P.T. acknowledges the scholarship from Chinese Scholarship Council (CSC). H.J.B. acknowledges funding from the European Research Council (ERC) under the European Union's Horizon 2020 research and innovation programme (grant agreement no. 834431) and the Spanish Ministry of Economy and Competitiveness (MINECO) via the Unidad de Excelencia María de Maeztu CEX2019-000919-M and MAT2017-88821-R. A.S., S.N. and R.H.F. acknowledge support from the UKRI Global Challenge Research Fund project, SUNRISE (EP/P032591/1) and UKIERI projects. S.N. acknowledges funding and support from Royal Society-SERB Newton International Fellowship.

Author contributions

Y.-H.K., S.K. and A.K. equally contributed to this work. Y.-H.K., S.K. and T.-W.L. initiated and designed the study. Y.-H.K. and S.K. performed experiments and analysed data. A.K., R.B.W. and P.T. performed the simulations, analysed data, helped understand the structures and mechanisms behind the great efficiency. J.P., D.-H.K. and S.H.J. helped to analyse the data. H.X. and B.H. performed and analysed magnetic field-dependent characteristics. Y.-H.L. and Y.-W.K. measured and analysed TEM. L.M.-S. and H.J.B. commented on the synthesis of nanocrystals. J.P. (KAIST) and S.Y. performed optical simulation of the devices. A.S., S.N. and R.H.F. performed the PLQE measurements and analysis. A.M.R. and T.-W.L. supervised the study. All authors discussed the results and commented on the manuscript.

Competing interests

The authors declare no competing interests.

Additional information

Supplementary information is available for this paper at <https://doi.org/10.1038/s41566-020-00732-4>.

Correspondence and requests for materials should be addressed to A.M.R. or T.-W.L.

Peer review information *Nature Photonics* thanks the anonymous reviewers for their contribution to the peer review of this work.

Reprints and permissions information is available at www.nature.com/reprints.